arXiv:1905.04229v1 [astro-ph.HE] 10 May 2019

Direct Measurement of the Cosmic-Ray Proton Spectrum from 50 GeV to 10 TeV with the Calorimetric Electron Telescope on the International Space Station

O. Adriani,[1,2] Y. Akaike,[3,4] K. Asano,[5] Y. Asaoka,[6,7,*] M.G. Bagliesi,[8,9] E. Berti,[1,2] G. Bigongiari,[8,9] W.R. Binns,[10] S. Bonechi,[8,9] M. Bongi,[1,2] A. Bruno,[11] J.H. Buckley,[10] N. Cannady,[12] G. Castellini,[13] C. Checchia,[14,15] M.L. Cherry,[12] G. Collazuol,[14,15] V. Di Felice,[16,17] K. Ebisawa,[18] H. Fuke,[18] T.G. Guzik,[12] T. Hams,[3,19] N. Hasebe,[6] K. Hibino,[20] M. Ichimura,[21] K. Ioka,[22] W. Ishizaki,[5] M.H. Israel,[10] K. Kasahara,[6] J. Kataoka,[6] R. Kataoka,[23] Y. Katayose,[24] C. Kato,[25] N. Kawanaka,[26,27] Y. Kawakubo,[12,28] K. Kohri,[29] H.S. Krawczynski,[10] J.F. Krizmanic,[19,3] T. Lomtadze,[9] P. Maestro,[8,9] P.S. Marrocchesi,[8,9,†] A.M. Messineo,[30,9] J.W. Mitchell,[4] S. Miyake,[31] A.A. Moiseev,[32,19] K. Mori,[6,18] M. Mori,[33] N. Mori,[2] H.M. Motz,[34] K. Munakata,[25] H. Murakami,[6] S. Nakahira,[35] J. Nishimura,[18] G.A. de Nolfo,[11] S. Okuno,[20] J.F. Ormes,[36] S. Ozawa,[6] L. Pacini,[1,13,2] F. Palma,[16,17] P. Papini,[2] A.V. Penacchioni,[8,37] B.F. Rauch,[10] S.B. Ricciarini,[13,2] K. Sakai,[19,3] T. Sakamoto,[28] M. Sasaki,[19,32] Y. Shimizu,[20] A. Shiomi,[38] R. Sparvoli,[16,17] P. Spillantini,[1] F. Stolzi,[8,9] J.E. Suh,[8,9] A. Sulaj,[8,9] I. Takahashi,[39] M. Takayanagi,[18] M. Takita,[5] T. Tamura,[20] T. Terasawa,[35] H. Tomida,[18] S. Torii,[6,40,‡] Y. Tsunesada,[41] Y. Uchihori,[42] S. Ueno,[18] E. Vannuccini,[2] J.P. Wefel,[12] K. Yamaoka,[43] S. Yanagita,[44] A. Yoshida,[28] and K. Yoshida[45]

(CALET Collaboration)

[1] *Department of Physics, University of Florence, Via Sansone, 1 - 50019 Sesto, Fiorentino, Italy*
[2] *INFN Sezione di Florence, Via Sansone, 1 - 50019 Sesto, Fiorentino, Italy*
[3] *Department of Physics, University of Maryland, Baltimore County, 1000 Hilltop Circle, Baltimore, Maryland 21250, USA*
[4] *Astroparticle Physics Laboratory, NASA/GSFC, Greenbelt, Maryland 20771, USA*
[5] *Institute for Cosmic Ray Research, The University of Tokyo, 5-1-5 Kashiwa-no-Ha, Kashiwa, Chiba 277-8582, Japan*
[6] *Waseda Research Institute for Science and Engineering, Waseda University, 3-4-1 Okubo, Shinjuku, Tokyo 169-8555, Japan*
[7] *JEM Utilization Center, Human Spaceflight Technology Directorate, Japan Aerospace Exploration Agency, 2-1-1 Sengen, Tsukuba, Ibaraki 305-8505, Japan*
[8] *Department of Physical Sciences, Earth and Environment, University of Siena, via Roma 56, 53100 Siena, Italy*
[9] *INFN Sezione di Pisa, Polo Fibonacci, Largo B. Pontecorvo, 3 - 56127 Pisa, Italy*
[10] *Department of Physics and McDonnell Center for the Space Sciences, Washington University, One Brookings Drive, St. Louis, Missouri 63130-4899, USA*
[11] *Heliospheric Physics Laboratory, NASA/GSFC, Greenbelt, Maryland 20771, USA*
[12] *Department of Physics and Astronomy, Louisiana State University, 202 Nicholson Hall, Baton Rouge, Louisiana 70803, USA*
[13] *Institute of Applied Physics (IFAC), National Research Council (CNR), Via Madonna del Piano, 10, 50019 Sesto, Fiorentino, Italy*
[14] *Department of Physics and Astronomy, University of Padova, Via Marzolo, 8, 35131 Padova, Italy*
[15] *INFN Sezione di Padova, Via Marzolo, 8, 35131 Padova, Italy*
[16] *University of Rome "Tor Vergata", Via della Ricerca Scientifica 1, 00133 Rome, Italy*
[17] *INFN Sezione di Rome "Tor Vergata", Via della Ricerca Scientifica 1, 00133 Rome, Italy*
[18] *Institute of Space and Astronautical Science, Japan Aerospace Exploration Agency, 3-1-1 Yoshinodai, Chuo, Sagamihara, Kanagawa 252-5210, Japan*
[19] *CRESST and Astroparticle Physics Laboratory NASA/GSFC, Greenbelt, Maryland 20771, USA*
[20] *Kanagawa University, 3-27-1 Rokkakubashi, Kanagawa, Yokohama, Kanagawa 221-8686, Japan*
[21] *Faculty of Science and Technology, Graduate School of Science and Technology, Hirosaki University, 3, Bunkyo, Hirosaki, Aomori 036-8561, Japan*
[22] *Yukawa Institute for Theoretical Physics, Kyoto University, Kitashirakawa Oiwakecho, Sakyo, Kyoto 606-8502, Japan*
[23] *National Institute of Polar Research, 10-3, Midori-cho, Tachikawa, Tokyo 190-8518, Japan*
[24] *Faculty of Engineering, Division of Intelligent Systems Engineering, Yokohama National University, 79-5 Tokiwadai, Hodogaya, Yokohama 240-8501, Japan*
[25] *Faculty of Science, Shinshu University, 3-1-1 Asahi, Matsumoto, Nagano 390-8621, Japan*
[26] *Hakubi Center, Kyoto University, Yoshida Honmachi, Sakyo-ku, Kyoto 606-8501, Japan*
[27] *Department of Astronomy, Graduate School of Science, Kyoto University, Kitashirakawa Oiwake-cho, Sakyo-ku, Kyoto 606-8502, Japan*

[28] College of Science and Engineering, Department of Physics and Mathematics,
Aoyama Gakuin University, 5-10-1 Fuchinobe, Chuo, Sagamihara, Kanagawa 252-5258, Japan
[29] Institute of Particle and Nuclear Studies, High Energy Accelerator
Research Organization, 1-1 Oho, Tsukuba, Ibaraki 305-0801, Japan
[30] University of Pisa, Polo Fibonacci, Largo B. Pontecorvo, 3 - 56127 Pisa, Italy
[31] Department of Electrical and Electronic Systems Engineering,
National Institute of Technology, Ibaraki College,
866 Nakane, Hitachinaka, Ibaraki 312-8508 Japan
[32] Department of Astronomy, University of Maryland, College Park, Maryland 20742, USA
[33] Department of Physical Sciences, College of Science and Engineering, Ritsumeikan University, Shiga 525-8577, Japan
[34] Faculty of Science and Engineering, Global Center for Science and Engineering,
Waseda University, 3-4-1 Okubo, Shinjuku, Tokyo 169-8555, Japan
[35] RIKEN, 2-1 Hirosawa, Wako, Saitama 351-0198, Japan
[36] Department of Physics and Astronomy, University of Denver, Physics Building,
Room 211, 2112 East Wesley Avenue, Denver, Colorado 80208-6900, USA
[37] ASI Science Data Center (ASDC), Via del Politecnico snc, 00133 Rome, Italy
[38] College of Industrial Technology, Nihon University, 1-2-1 Izumi, Narashino, Chiba 275-8575, Japan
[39] Kavli Institute for the Physics and Mathematics of the Universe,
The University of Tokyo, 5-1-5 Kashiwanoha, Kashiwa, 277-8583, Japan
[40] School of Advanced Science and Engineering, Waseda University, 3-4-1 Okubo, Shinjuku, Tokyo 169-8555, Japan
[41] Division of Mathematics and Physics, Graduate School of Science,
Osaka City University, 3-3-138 Sugimoto, Sumiyoshi, Osaka 558-8585, Japan
[42] National Institutes for Quantum and Radiation Science and Technology, 4-9-1 Anagawa, Inage, Chiba 263-8555, Japan
[43] Nagoya University, Furo, Chikusa, Nagoya 464-8601, Japan
[44] College of Science, Ibaraki University, 2-1-1 Bunkyo, Mito, Ibaraki 310-8512, Japan
[45] Department of Electronic Information Systems, Shibaura Institute of Technology,
307 Fukasaku, Minuma, Saitama 337-8570, Japan

(Dated: March 17, 2022)

In this paper, we present the analysis and results of a direct measurement of the cosmic-ray proton spectrum with the CALET instrument onboard the International Space Station, including the detailed assessment of systematic uncertainties. The observation period used in this analysis is from October 13, 2015 to August 31, 2018 (1054 days). We have achieved the very wide energy range necessary to carry out measurements of the spectrum from 50 GeV to 10 TeV covering, for the first time in space, with a single instrument the whole energy interval previously investigated in most cases in separate subranges by magnetic spectrometers (BESS-TeV, PAMELA, and AMS-02) and calorimetric instruments (ATIC, CREAM, and NUCLEON). The observed spectrum is consistent with AMS-02 but extends to nearly an order of magnitude higher energy, showing a very smooth transition of the power-law spectral index from -2.81 ± 0.03 (50–500 GeV) neglecting solar modulation effects (or -2.87 ± 0.06 including solar modulation effects in the lower energy region) to -2.56 ± 0.04 (1–10 TeV), thereby confirming the existence of spectral hardening and providing evidence of a deviation from a single power law by more than 3σ.

PACS numbers: 96.50.sb,95.35.+d,95.85.Ry,98.70.Sa,29.40.Vj

INTRODUCTION

Direct measurements of the high-energy spectra of each species of cosmic-ray nuclei up to the PeV energy scale provide detailed insight into the general phenomenology of cosmic-ray acceleration and propagation in the Galaxy. A possible charge-dependent cutoff in the nuclei spectra is hypothesized to explain the "knee" in the all-particle spectrum. This hypothesis can be tested directly with measurements by long duration space experiments with sufficient exposure and with the capability of identifying individual elements based on charge measurements.

Furthermore, the spectral hardening observed in the spectra of various nuclei [1–11] calls for the extensive attempts [12–32] to theoretically interpret these unexpected phenomena. The current experimental approaches to direct measurements of the proton spectrum are based on two main classes of instruments, i.e., magnetic spectrometers [5, 6] at lower energies where the presence of a spectral breakpoint was observed, and calorimeters [1, 4, 8, 33, 34] at higher energies where the spectrum undergoes a hardening. It is of particular interest to determine the onset of spectral hardening and its development in terms of index variation and smoothness parameter (as defined in Ref. [6]). In order to achieve a consistent picture, measurements should be unaffected, as much as possible, by systematic errors and a critical comparison of the observations from different experiments is in order.

The CALorimetric Electron Telescope (CALET) [35, 36], a space-based instrument optimized for the measurement of the all-electron spectrum [37, 38] and equipped

with a fully active calorimeter, can measure the main components of cosmic rays including proton, light and heavy nuclei (up to iron and above) in the energy range up to ∼1 PeV. The thickness of the calorimeter corresponds to 30 radiation length (at normal incidence) and to ∼1.3 proton interaction length.

In this Letter, we present a direct measurement of the cosmic-ray proton spectrum from $E = 50$ GeV to 10 TeV with CALET where E denotes the kinetic energy of primary protons throughout this paper. Its wide dynamic range allows the study of the detailed shape of the spectrum by using a single instrument.

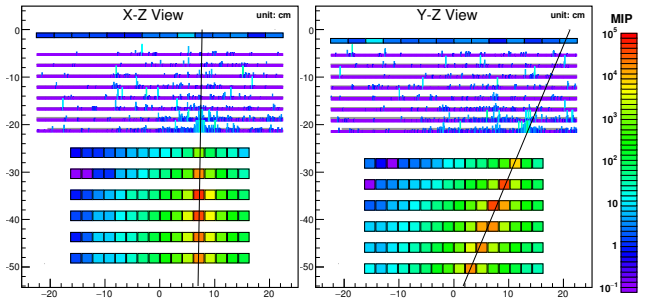


FIG. 1. An example of a high-energy proton event with an energy deposit sum of 10 TeV. Black lines represent the reconstructed tracks using Kalman Filter tracking [40], which achieves a fine resolution taking advantage of the high granularity of the IMC.

CALET INSTRUMENT

CALET consists of a charge detector (CHD), a 3 radiation-length thick imaging calorimeter (IMC) and a 27 radiation-length thick total absorption calorimeter (TASC), with a field of view of ∼45° from zenith. A "fiducial" geometrical factor of ∼416 cm^{2}sr for particles penetrating CHD top to TASC bottom, with 2 cm margins at the first and the last TASC layers (Acceptance A), and corresponding to about 40% of the total acceptance [38], is used in this analysis.

The CHD, which identifies the charge of the incident particle, is comprised of a pair of plastic scintillator hodoscopes arranged in two orthogonal layers. The IMC is a sampling calorimeter alternating thin layers of Tungsten absorber with layers of scintillating fibers read-out individually, also providing an independent charge measurement via multiple dE/dx samples. The TASC is a tightly packed lead-tungstate ($PbWO_4$) hodoscope, measuring the energy of showering particles in the detector. A very large dynamic range of more than 6 orders of magnitude is covered by four different gain ranges [39]. A more complete description of the instrument is given in the Supplemental Material of Ref. [37].

Figure 1 shows a proton candidate with energy deposit of ∼10 TeV in the detector. The event example clearly demonstrates CALET's capability to reconstruct and identify very high energy protons. Because of the limited energy resolution, energy unfolding is required to estimate the primary energy distribution. It is important, therefore, to infer the detector response at the highest energies covered by the analysis.

The instrument was launched on August 19, 2015 and emplaced on the Japanese Experiment Module-Exposed Facility on the International Space Station with an expected mission duration of five years (or more). Scientific observations [36] started on October 13, 2015, and smooth and continuous operations have taken place since then.

DATA ANALYSIS

We have analyzed flight data collected for 1054 days from October 13, 2015 to August 31, 2018. The total observation live time for high-energy (HE) shower trigger [36] is 21421.9 hours and live time fraction to total time is 84.7%. In addition, the low-energy (LE) shower trigger operated at a high geomagnetic latitude [36] is used to extend the energy coverage toward the lower energy region. In spite of a limited live time of 365.4 hr, LE data provide sufficient statistics for protons below a few hundred GeV.

Monte Carlo (MC) simulations, reproducing the detailed detector configuration, physics processes, as well as detector signals, are based on the EPICS simulation package [41, 42].

In order to assess the relatively large uncertainties in the hadronic interactions, a series of beam tests were carried out at CERN-SPS using the CALET beam test model [43–45]. Trigger efficiency and energy response derived from MC simulations were tuned using the beam test results obtained in 2012 [43, 44, 46] with proton beams of 30, 100 and 400 GeV. The correction for the trigger efficiency obtained by the EPICS simulation was determined to be 7.7% for the LE trigger and 11.2% for the HE trigger, irrespective of proton energies. Shower energy correction was determined to be 7.9% and 6.3% at 30 and 100 GeV, and no correction at 400 GeV and above, where simple log-linear interpolation was used to determine the correction factor for intermediate energies.

In the analysis of hadrons, especially in the high-energy region where no beam test calibration is possible, a comparison between different MC models becomes much more important than in electron analysis. For this purpose, we have run simulations with FLUKA [47–49] and Geant4 [50, 51] in the same way as EPICS. The detector models used in FLUKA and Geant4 are almost identical to the CALET CAD model used in EPICS.

In electron analysis [37, 38], the electromagnetic shower tracking algorithm works very well, because of the presence of a developed shower core that is used as an initial guess of the trajectory of the incoming particle. In the proton analysis, however, the hadronic interaction occurs abruptly and there is no guarantee of the presence of a well-developed shower core in the bottom two layers of the IMC. It is therefore necessary to follow a different approach to reconstruct the proton tracks in a highly efficient way. Combinatorial Kalman Filter tracking [40] was developed for this purpose and it is used in the proton spectrum analysis described hereafter.

The shower energy of each event is calculated as the TASC energy deposit sum (observed energy: $E_{\rm TASC}$), which is calibrated using penetrating particles and by performing a seamless stitching of adjacent gain ranges on orbit, complemented by the confirmation of the linearity of the system over the whole range by means of ground measurements using UV pulse laser as described in Ref. [39]. Temporal variations during the long-term observation are also corrected, sensor by sensor, using penetrating particles as gain monitor [37].

In order to minimize helium contamination by accurately separating protons from helium based on their charge, a preselection of well-reconstructed and well-contained events is applied. Preselection consists of (1) offline trigger confirmation, (2) geometrical condition (requires Acceptance A [38]), (3) track quality cut to ensure reliability of the reconstructed track while retaining high efficiency, (4) electron rejection cut, (5) off-acceptance events rejection cut, (6) requirement of track consistency with TASC energy deposits, and (7) shower development requirement in the IMC. Some of the above selections are described in more detail in the following.

Consistency between MC and flight data (FD) for triggered events is obtained by an offline trigger, which requires more severe conditions than the onboard trigger. It removes non-negligible effects due to positional and temporal variation of the detector gain, and it is applied as a first step of preselection.

In order to reject electronlike events, a "Moliere concentration" along the track in the IMC is calculated by summing up all energy deposits found inside one Moliere radius for Tungsten ($\pm$9 fibers, i.e., 9 mm) around the fiber matched with the track, and normalized to the total energy deposit sum in the IMC. By requiring this quantity to be less than 0.7, most of electrons are rejected while retaining an efficiency above 92% for protons.

Because of the nature of hadronic interaction and combinatorial track reconstruction, there is a possibility to introduce a misreconstruction by erroneously identifying one of the secondary tracks as the primary track. To minimize the fraction of misidentified events, two topological cuts are applied using TASC energy-deposit information irrespective of IMC tracking.

Further rejection is achieved with a consistency cut between the track impact point and center of gravity of energy deposits in the first (TASC-X1) and second (TASC-Y1) layers of the TASC. Energy dependent thresholds are defined using MC simulation to have a constant efficiency of 95% for events that interacted in the IMC below the fourth layer, which are suitable for determining charge, energy, and trigger efficiency (hereafter denoted as "target" events).

Backscattered particles produced in the shower affect both the trigger and the charge determination. Primary particles below the trigger thresholds might be triggered anyway because of backscattered particles hitting TASC-X1 and IMC bottom layers. Moreover the large amount of shower particle tracks backscattered from TASC may induce fake charge identification by releasing additional amounts of energy that add up to the primary particle ionization signal, resulting in a shift of the charge distribution and a larger width.

Since a fraction of events triggered by backscattering is not reproduced well by the simulations, rejection of such events is important. For this purpose, the energy deposit sum along the shower axis over $\pm$9 fibers (in total 19 fibers) is used to ensure the existence of a shower core in the IMC. This definition differs from the one used for electrons considering the wider lateral spread of hadronic showers. In order to fully exploit the rejection capability of events triggered by backscattering, it is important to set an appropriate threshold as a function of energy. Energy dependent thresholds are defined to get 99% efficiency for "target" events.

The identification of cosmic-ray nuclei via a measurement of their charge is carried out with two independent subsystems that are routinely used to cross-calibrate each other: the CHD and the IMC [52]. The latter samples the ionization deposits in each layer, thereby providing a multiple dE/dx measurement with a maximum of 16 samples along the track. The interaction point is first reconstructed [53] and only the dE/dx ionization clusters from the layers upstream the interaction point are used. The charge value is evaluated as a truncated mean of the valid samples with a truncation level set at 70%.

To mitigate the backscattering effects, an energy dependent charge correction to restore the nominal peak positions of protons and helium to $Z = 1$ and 2 is applied separately to FD, EPICS, FLUKA and Geant4, where the same correction is used for both protons and helium. Charge selection of proton and helium candidates is performed by applying simultaneous window cuts on CHD and IMC reconstructed charges. The resultant charge distributions are exemplified in Fig. 2. For the selection with the CHD and IMC, energy dependent thresholds are defined separately for the CHD and IMC to keep 95% efficiency for "target" events.

In the lower energy region, the use of the LE trigger is necessary to avoid trigger threshold bias due to the sharp drop in efficiency at $E < 100$ GeV, an effect that

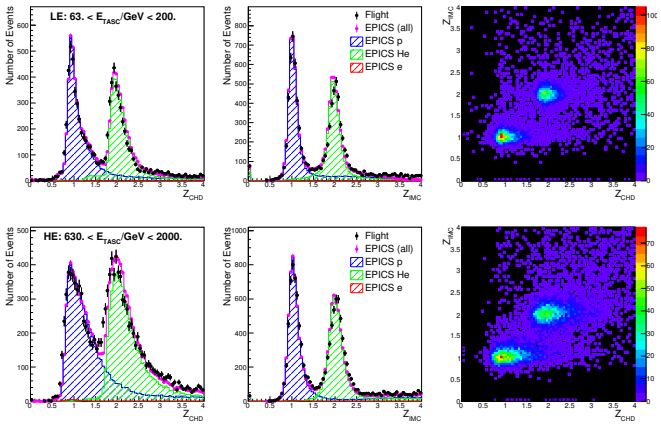


FIG. 2. Examples of CHD/IMC charge distributions. Left, center, and right panels show the CHD charge, IMC charge and correlation between CHD and IMC charges, respectively. Top and bottom plots correspond to events with $63 < E_{\rm TASC} < 200$ GeV and $630 < E_{\rm TASC} < 2000$ GeV, respectively. An enlarged version of the figure is available as Fig. S1 in the Supplemental Material [54].

extends to the higher energy region via the energy unfolding procedure. With the exception of the offline trigger confirmation threshold which is adjusted to match the hardware trigger, the event selection criteria used in HE and LE analyses are identical. Figure 3 shows the effective acceptance of LE- and HE-trigger analyses after applying all the selection criteria. While the overall difference between the two analyses is rather small, the difference in the low-energy region is sizable.

Background contamination is estimated from the MC simulation of protons, helium, and electrons as a function of observed energy. Among them, the dominant component is off-acceptance protons except for the highest energy region $E_{\rm TASC} \sim 10$ TeV, where helium contamination becomes dominant. Overall contamination is estimated below a few percent, and at maximum ∼5% in

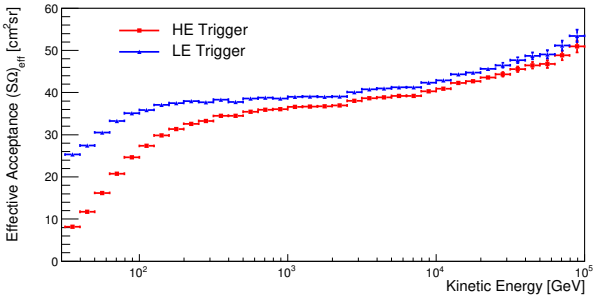


FIG. 3. Comparison of effective acceptance for HE-trigger (red) and LE-trigger (blue) analyses. obtained by MC simulation. The difference between the two selections is the offline trigger confirmation only.

the lowest and highest energy region. The correction is carried out before performing the energy unfolding procedure, which is described in the following.

In order to take into account the relatively limited energy resolution (observed energy fraction is around 35% and the resultant energy resolution is 30%–40%), energy unfolding is necessary to correct for bin-to-bin migration effects. In this analysis, we used the Bayesian approach implemented in the RooUnfold package [55, 56] in ROOT [57], with the response matrix derived using MC simulation. Convergence is obtained within two iterations, given the relatively accurate prior distribution obtained from the previous observations, i.e., AMS-02 [6] and CREAM-III [8].

The proton spectrum is obtained by correcting the effective geometrical acceptance with the unfolded energy distribution as follows:

$$\Phi(E) = \frac{n(E)}{(S\Omega)_{\rm eff}(E)\ T\,\Delta E},$$
$$n(E) = U\big(n_{\rm obs}(E_{\rm TASC}) - n_{\rm bg}(E_{\rm TASC})\big),$$

where ΔE denotes the energy bin width, $U()$ the unfolding procedure based on Bayes theorem, $n(E)$ the bin counts of the unfolded distribution, $n_{\rm obs}(E_{\rm TASC})$ those of observed energy distribution (including background), $n_{\rm bg}(E_{\rm TASC})$ the bin counts of background events in the observed energy distribution, $(S\Omega)_{\rm eff}$ the effective acceptance including all selection efficiencies, and T the live time.

Depending on the on-orbit trigger mode and corresponding offline-trigger threshold, two spectra are obtained with the LE and HE analyses, respectively, as shown in Fig. S2 in the Supplemental Material [54]. For $E < 200$ GeV, the use of LE-trigger analysis is required because an offline trigger threshold higher than in the hardware trigger was found to introduce an efficiency bias in the HE-trigger analysis, which became evident with a scan of the offline-trigger threshold using LE-trigger data. Since both fluxes are well consistent in $E > 200$ GeV, they are combined around $E \sim 300$ GeV, taking into account the different statistics of the two trigger modes.

SYSTEMATIC UNCERTAINTIES

Dominant sources of systematic uncertainties in proton analysis include (1) hadronic interaction modeling, (2) energy response, (3) track reconstruction, and (4) charge identification. To address these uncertainties, various approaches are used as discussed in the Supplemental Material [54]. An important part of systematics comes from the accuracy of the beam test calibration and its extrapolation or interpolation. The stability of the measured spectrum against variations of several analysis cuts is also a crucial tool to estimate the associated uncertainties.

Considering all of the above contributions, the total systematic uncertainty, as summarized in Fig. S4 in the Supplemental Material [54], is within 10% and estimated separately for normalization and energy dependent uncertainties.

RESULTS

Figure 4 shows the proton spectrum measured with CALET in an energy range from 50 GeV to 10 TeV, where current uncertainties that include statistical and systematic errors are bounded within a gray band. The measured proton flux and the statistical and systematic errors are tabulated in Table I of the Supplemental Material [54]. In Fig. 4, the CALET spectrum is compared with recent experiments from space (PAMELA [59, 60], AMS-02 [6], and NUCLEON [34]) and from the high altitude balloon experiments (BESS-TeV [58], ATIC-2 [1], CREAM-I [4], and CREAM-III [8]). Our spectrum is in good agreement with the very accurate magnetic spectrometer measurements by AMS-02 in the low-energy region, and the spectral behavior is also consistent with measurements from calorimetric instruments in the higher energy region.

Figure 5 (a) shows the fits of the CALET proton spectrum with a single power law. In order to study the spectral behavior, only the energy dependent systematics are included in the data points. Red, blue, and magenta lines indicate the fit result for the energy intervals between 50 and 500 GeV, 1 and 10 TeV, and 50 GeV and 10 TeV, respectively. The fit yields $\gamma_1 = -2.81 \pm 0.03$ at lower energy (neglecting solar modulation effects) and $\gamma_2 = -2.56 \pm 0.04$ at higher energy with good chi-square

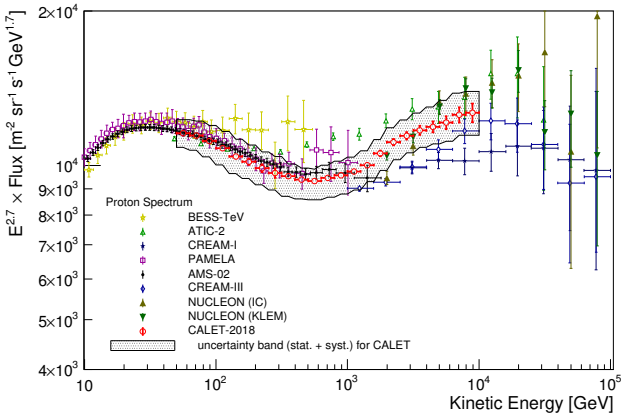


FIG. 4. Cosmic-ray proton spectrum measured by CALET (red points) from 50 GeV to 10 TeV. The gray band indicates the quadratic sum of statistical and systematic errors. Also plotted are recent direct measurements [1, 4, 6, 8, 34, 58–60]. An enlarged version of the figure is available as Fig. S6 in the Supplemental Material [54].

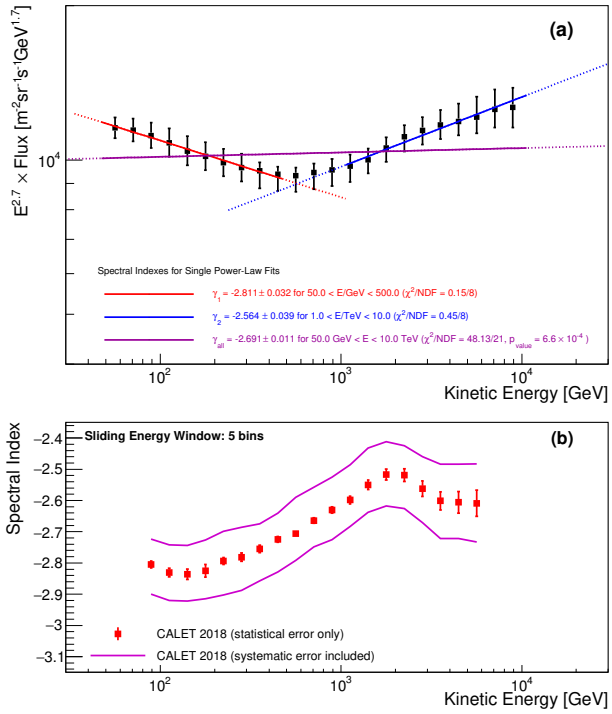


FIG. 5. (a) Fit of the CALET proton spectrum with single power-law functions. Red, blue, and magenta lines indicate the fit result for the energy ranges between 50 and 500 GeV, 1 and 10 TeV, and 50 GeV and 10 TeV, respectively. (b) Energy dependence of the spectral index calculated within a sliding energy window for CALET (red squares). The spectral index is determined for each bin by fitting the data using ±2 energy bins. Magenta curves indicate the uncertainty range including systematic errors.

values. On the other hand, the whole range fit gives a large chi-square per degree of freedom, disfavoring the single power-law hypothesis by more than 3σ. Our spectrum can also be fitted with a smoothly broken power-law function [6, 61] as shown in Fig. S7 of the Supplemental Material [54], resulting in a power-law index of -2.87 ± 0.06 (including solar modulation effects) below the breakpoint rigidity, which is in good agreement with AMS-02 [6]. A larger variation of the power-law index of 0.30 ± 0.08 and a higher breakpoint rigidity of 496 ± 175 GV than AMS-02 [6] are observed, though the latter is affected by relatively large error.

Furthermore, Fig.5 (b) shows the energy dependence of the spectral index calculated within a sliding energy window (red squares). The spectral index is determined for each bin by a fit of the data including the neighbor ±2 bins. Magenta curves indicate the uncertainty band including systematic errors. This result confirms a clear hardening of the spectrum above a few hundred GeV. These results may be important for the interpretation of the proton spectrum (e.g. [17, 18, 31]), since they indicate a progressive hardening up to the TeV region, while in

good agreement with magnet spectrometers in the 100 GeV to sub-TeV region.

CONCLUSION

We have measured, for the first time with an experimental apparatus in low Earth Orbit, the cosmic-ray proton spectrum from 50 GeV to 10 TeV, covering with a single instrument the whole energy range previously investigated by magnetic spectrometers (BESS-TEV, PAMELA and AMS-02) and calorimetric instruments (ATIC, CREAM and NUCLEON) covering, in most of the cases, separate subranges of the region explored so far by CALET. Our observations confirm the presence of a spectral hardening above a few hundred GeV. Our spectrum is not consistent with a single power law covering the whole range, while both 50–500 GeV and 1–10 TeV subranges can be separately fitted with single power-law functions, with the spectral index of the lower (higher) energy region being consistent with AMS-02 [6] (CREAM-III [8]) within errors. With the observation of a smoothly broken power law and of an energy dependence of the spectral index, CALET's proton spectrum will contribute to shed light on the origin of the spectral hardening. Improved statistics and better understanding of the instrument based on the analysis of additional flight data during the ongoing five years (or more) of observations might reveal a charge dependent energy cutoff possibly due to the acceleration limit in supernova remnants in proton and helium spectra, or set important constraints on the acceleration models.

ACKNOWLEDGMENTS

We gratefully acknowledge JAXA's contributions to the development of CALET and to the operations onboard the International Space Station. We also express our sincere gratitude to ASI and NASA for their support of the CALET project. This work was supported in part by JSPS Grant-in-Aid for Scientific Research (S) Grant No. 26220708, JSPS Grant-in-Aid for Scientific Research (B) Grant No. 17H02901, and by the MEXT-Supported Program for the Strategic Research Foundation at Private Universities (2011–2015) (Grant No. S1101021) at Waseda University. The CALET effort in the United States is supported by NASA through Grants No. NNX16AB99G, No. NNX16AC02G, and No. NNH14ZDA001N-APRA-0075.

* yoichi.asaoka@aoni.waseda.jp
† piersimone.marrocchesi@pi.infn.it
‡ torii.shoji@waseda.jp

[1] A. Panov *et al.*, Bull. Russ. Acad. Sci. Phys. **71**, 494 (2007) .
[2] H. Ahn *et al.*, Astrophys. J. **707**, 593 (2009) .
[3] H. Ahn *et al.*, Astrophys. J. Lett. **714**, L89 (2010) .
[4] Y. Yoon *et al.*, Astrophys. J. **728**, 122 (2011) .
[5] O. Adriani *et al.*, Science **332**, 69 (2011) .
[6] M. Aguilar *et al.* (AMS Collaboration), Phys. Rev. Lett. **114**, 171103 (2015) .
[7] M. Aguilar *et al.* (AMS Collaboration), Phys. Rev. Lett. **115**, 211101 (2015) .
[8] Y. Yoon *et al.*, Astrophys. J. **839**, 5 (2017) .
[9] M. Aguilar *et al.* (AMS Collaboration), Phys. Rev. Lett. **119**, 251101 (2017) .
[10] M. Aguilar *et al.* (AMS Collaboration), Phys. Rev. Lett. **120**, 021101 (2018) .
[11] M. Aguilar *et al.* (AMS Collaboration), Phys. Rev. Lett. **121**, 051103 (2018) .
[12] D. Ellison *et al.*, Astrophys. J. **487**, 197 (1997) .
[13] M. A. Malkov, P. H. Diamond, and R. Z. Sagdeev, Phys. Rev. Lett. **108**, 081104 (2012) .
[14] A. Erlykin and A. Wolfendale, Astropart. Phys. **35**, 449 (2012) .
[15] Thoudam and J. Hörandel, Mon. Not. R. Astron Soc. **421**, 1209 (2012) .
[16] G. Bernard *et al.*, Astron. Astrophys. **555**, A48 (2013) .
[17] P. Blasi, E. Amato, and P. D. Serpico, Phys. Rev. Lett. **109**, 061101 (2012) .
[18] R. Aloisio and P. Blasi, J. Cosmol. Astropart. Phys. **07**, 001 (2013) .
[19] V. Ptuskin, V. Zirakashvili, and E. Seo, in *Proceedings of the 32nd ICRC*, Vol. 6 (2011) p. 240 .
[20] S. Thoudam and J. Hörandel, Astron. Astrophys. **567**, A33 (2014) .
[21] L. Drury, Mon. Not. R. Astron Soc. **415**, 1807 (2011) .
[22] Y. Ohira and K. Ioka, Astrophys. J. Lett. **729**, L13 (2011) .
[23] Y. Ohira, N. Kawanaka, and K. Ioka, Phys. Rev. D **93**, 083001 (2016) .
[24] P. Biermann *et al.*, Astrophys. J. **725**, 184 (2010) .
[25] V. Ptuskin, V. Zirakashvili, and E. Seo, Astrophys. J. **763**, 47 (2013) .
[26] V. Zatsepin and N. Sokolskaya, Astron. Astrophys. **458**, 1 (2006) .
[27] N. Tomassetti, Astrophys. J. Lett. **752**, L13 (2012) .
[28] A. Vladimirov, G. Jóhannesson, I. Moskalenko, and T. Porter, Astrophys. J. **752**, 68 (2012) .
[29] N. Tomassetti, Phys. Rev. D **92**, 063001 (2015) .
[30] G. Giacinti, M. Kachelrieß, and D. Semikoz, J. Cosmol. Astropart. Phys. **07**, 051 (2018) .
[31] C. Evoli, P. Blasi, G. Morlino, and R. Aloisio, Phys. Rev. Lett. **121**, 021102 (2018) .
[32] N. Kawanaka and S. Yanagita, Phys. Rev. Lett. **120**, 041103 (2018) .
[33] E. Atkin *et al.*, JCAP **07**, 020 (2017) .
[34] E. Atkin *et al.*, JETP Letters **108**, 5 (2018) .
[35] S. Torii *et al.* (CALET Collaboration), in *Proceeding of Science (ICRC2017) 1092* (2017) .
[36] Y. Asaoka, Y. Ozawa, S. Torii, *et al.* (CALET Collaboration), Astropart. Phys. **100**, 29 (2018) .
[37] O. Adriani *et al.* (CALET Collaboration), Phys. Rev. Lett. **119**, 181101 (2017) .
[38] O. Adriani *et al.* (CALET Collaboration), Phys. Rev. Lett. **120**, 261102 (2018) .

[39] Y. Asaoka, Y. Akaike, Y. Komiya, R. Miyata, S. Torii, *et al.* (CALET Collaboration), Astropart. Phys. **91**, 1 (2017) .

[40] P. Maestro, N. Mori, *et al.* (CALET Collaboration), in *Proceedings of Science (ICRC2017) 208* (2017) .

[41] K. Kasahara, in *Proc. of 24th international cosmic ray conference (Rome, Italy)*, Vol. 1 (1995) p. 399 .

[42] EPICS and COSMOS versions are 9.20 and 8.00, respectively .

[43] Y. Akaike *et al.* (CALET Collaboration), in *Proc. of 33rd international cosmic ray conference (ICRC2013) 726* (2013) .

[44] T. Niita, S. Torii, Y. Akaike, Y. Asaoka, K. Kasahara, *et al.*, Adv. Space Res. **55**, 2500 (2015) .

[45] Y. Akaike *et al.* (CALET Collaboration), in *Proceeding of Sciences (ICRC2015) 613* (2015) .

[46] T. Tamura *et al.*, to be published .

[47] T. Böhlen, Nuclear Data Sheets **120**, 211 (2014) .

[48] A. Ferrari, P. Sala, A. Fassó, and J. Ranft, in *INFN/TC_05/11, SLAC-R-773, CERN-2005-10* (2005) .

[49] The version of FLUKA is Fluka2011.2c.4 .

[50] S. Agostinelli *et al.*, Nucl. Instrum. Methods Phys. Res. **A506**, 250 (2003) .

[51] Geant4 version employs FTFP_BERT as a physics list which is recommended for the simulation of high energy showers .

[52] P. S. Marrocchesi *et al.* (CALET Collaboration), in *Proceeding of Science (ICRC2017) 156* (2017) .

[53] P. Brogi *et al.* (CALET Collaboration), in *Proceedings of Science (ICRC2015)* (2015) p. 585 .

[54] See the Supplemental Material at URL for supporting figures and the tabulated proton fluxes, as well as the description of data analysis procedure and the detailed assessment of systematic uncertainties .

[55] T. Adye, in *arXiv:1105.1160v1* (2011) .

[56] G. D'Agostini, *Nucl. Instrum. Methods Phys Res., Sect. A*, **362**, 487 (1995) .

[57] R. Brun and F. Rademakers, *Nucl. Instrum. Methods Phys Res., Sect. A*, **389**, 81 (1997) .

[58] S. Haino *et al.*, Phys. Lett. B **594**, 35 (2004) .

[59] O. Adriani *et al.*, Phys. Rept. **544**, 323 (2014) .

[60] O. Adriani *et al.*, Riv. Nuovo Cim. **40**, 1 (2017) .

[61] L. Glesson and W. Axford, Astrophys. J. **154**, 1011 (1968) .

Direct Measurement of the Cosmic-Ray Proton Spectrum from 50 GeV to 10 TeV with the Calorimetric Electron Telescope on the International Space Station

Supplemental material relative to "Direct Measurement of the Cosmic-Ray Proton Spectrum from 50 GeV to 10 TeV with the Calorimetric Electron Telescope on the International Space Station."

DATA ANALYSIS

We describe the analysis procedure in three steps as follows. Although some of the descriptions are duplicate with the main text, we have included them here for completeness.

Event Selection

The first step is selection of proton candidate events. The selection criteria to select proton events are optimized and defined using MC simulations consisting of protons, helium and electrons. The same criteria are applied to both of the Flight Data (FD) and MC data (MC).

In order to minimize and to accurately separate protons from helium in charge identification, it is important to preselect well reconstructed and well contained events. Furthermore, by removing events not included in the MC samples, i.e., those with incidence from zenith angle greater than 90° and mis-reconstructed events, event samples equivalent between FD and MC were obtained to be fed into charge identification. This is the most important purpose of the preselection, which consists of (1) offline trigger confirmation, (2) geometrical condition, (3) track quality cut, (4) electron rejection cut, (5) off-acceptance events rejection cut, (6) requirement of track consistency with TASC energy deposits, and (7) shower development requirement in IMC. Each of the above selections are described in more detail in the following, and finally the charge identification based on CHD and IMC energy deposits is described. For the detailed description of the detector components used in the event selections, readers are referred to the Supplemental Material of Ref. [S1] and/or Refs. [S2, S3].

(1) Offline trigger confirmation

A first event selection is the onboard high energy shower trigger (HE trigger). This trigger uses a simple trigger condition which selects showering particles above 10 GeV by requiring large energy deposits in the middle of the detector, i.e., energy deposit sums of IMC-X7+X8, IMC-Y7+Y8 and TASC-X1 to exceed certain thresholds in coincidence [S3]. Since the HE trigger is working onboard, it is affected by position dependence, temperature dependence, and temporal variation of the detector gain. In order to obtain consistency between MC and FD in a simple way by removing such complicated effects, an offline trigger is applied as a first step of preselection, which requires sufficiently severer conditions than the onboard HE trigger. After applying all the calibration, the offline trigger requires that the energy deposit sums of IMC-X7+X8, IMC-Y7+Y8 and TASC-X1 have to be greater than 50 MIP, 50 MIP and 100 MIP, respectively, where one MIP corresponds to the energy deposit of minimum ionizing vertical muons at 2 GeV, i.e. 1.66 MeV for CHD paddle, 0.145 MeV for IMC fiber and 20.47 MeV for TASC log.

When analyzing events triggered by low-energy (LE) trigger which selects showering particles above 1 GeV, the offline trigger confirmation uses lower thresholds, i.e., 5 MIP for IMC-X7+X8, IMC-Y7+Y8 and 10 MIP for TASC-X1.

(2) Geometrical condition

In order to ensure the accuracy of charge selection and energy measurement, it is required that the reconstructed track must pass through the whole detector, i.e., from CHD top to TASC bottom, with 2 cm margin from the sides

of the TASC, which is defined as Acceptance A. All the geometrical conditions are summarized in the Supplemental Material of Ref. [S4] for reference.

(3) Track quality cut

Combinatorial Kalman Filter (KF) tracking [S5] was developed to reconstruct the proton tracks in a highly efficient way, and is used in this analysis. In order to ensure track quality, the algorithm for the tracking is required to be KF tracking or shower fit in X-Z and Y-Z projection, and the χ^2 of the fits to be less than 10 in both projections.

(4) Electron rejection cut

In order to reject electrons especially in the lowest energy region, Moliere concentration along the track is defined as follows: for each IMC layer crossed by the track, a Moliere concentration is calculated summing all energy deposits found inside one Moliere radius ($\pm$9 fibers) of each fiber matched to the track. Then the energy deposit sum within one Moliere radius is divided by the total energy deposit sum in IMC. By requiring this quantity to be less than 0.7, most of electrons are rejected while keeping very high efficiency for protons.

(5) Off-acceptance events rejection cut

Off-acceptance events are defined as those reconstructed as Acceptance A, but for which the true acceptance does not fulfill the condition of Acceptance A. Rejection of such off-acceptance events are necessary to precisely determine geometrical acceptance. The off-acceptance events consist dominantly of protons and helium. Since off-acceptance helium might not be separated in the charge selection due to the fact that secondaries (mostly pions) have charge one, such helium contamination also needs to be minimized.

The off-acceptance cut uses two discrimination variables. The first variable is the maximum fractional energy deposit in a single TASC layer. It is required to be less than 0.4 to reject laterally incident events. This selection is especially effective for TASC-X1 because it is used for trigger. The second variable is the maximum energy deposit ratio of the edge logs to the maximum log in each layer. Events are rejected if this variable is greater than 0.4. This cut is effective to remove events which exit from the side of TASC. Those selections have very high efficiency while not depending on the track reconstruction.

(6) Requirement of track consistency with TASC energy deposits

In order to further reject mis-reconstructed events, a consistency cut is defined between tracks and centers of gravity of energy deposits in TASC-X1 and TASC-Y1 layers. Energy dependent thresholds are defined using MC simulation to have a constant efficiency of 95% for events that interacted in IMC below the 4th layer, which are suitable for determining charge, energy, and trigger efficiency (hereafter denoted as "target" events).

(7) shower development requirement in IMC

Since a fraction of events triggered by backscattering is not reproduced well by the simulations, rejection of such events is important. For this purpose, the energy deposit sum along the shower axis over $\pm$9 fibers (in total 19 fibers) is used to ensure the existence of a shower core in IMC. This definition differs from the one used for electrons considering the wider lateral spread of hadronic showers. In order to fully exploit the rejection capability of events triggered by backscattering, it is important to set an appropriate threshold as a function of energy. Energy dependent thresholds are defined to get 99% efficiency for "target" events.

Charge identification

Based on the preselected samples, charge identification is performed using the CHD and the IMC [S6]. The latter samples the ionization deposits in each layer, thereby providing a multiple $\mathrm{d}E/\mathrm{d}x$ measurement with a maximum of 16 samples along the track. The interaction point is first reconstructed [S7] and only the $\mathrm{d}E/\mathrm{d}x$ ionization clusters from the layers upstream the interaction point are used. The charge value is evaluated as a truncated-mean of the valid samples with a truncation level set at 70%.

To mitigate the backscattering effects, an energy dependent charge correction to restore the nominal peak positions of protons and helium to $Z = 1$ and 2 is applied separately to FD, EPICS, FLUKA and Geant4. Charge selection of proton and helium candidates is performed by applying simultaneous window cuts on CHD and IMC reconstructed charges. The resultant charge distributions are exemplified in Fig. S1. For the selection with CHD and IMC, energy dependent thresholds are defined separately to keep 95% efficiency for "target" events.

Background Contamination

Background contamination is estimated from the MC simulation of protons, helium and electrons as a function of observed energy, where the previous observations, i.e., AMS-02 [S8, S9] and CREAM-III [S10], are used to simulate their spectral shape. Among them, the dominant component is off-acceptance protons except for the highest energy region $E_{\mathrm{TASC}} \sim 10$ TeV, where helium contamination becomes dominant. Overall contamination is estimated below a few percent, and at maximum $\sim$5% in the lowest and highest energy region. The correction is carried out before performing the energy unfolding procedure.

In the lower energy region, the mis-reconstruction probability for protons is higher, due to the poorer reconstruction of the TASC shower axis caused by the less prolate shower shapes at these energies. For helium, this mis-reconstruction probability is much lower due to larger energy deposits in each hit produced by a primary track in IMC. This is the main reason behind the higher contamination ratio due to off-acceptance protons in the low energy region. In the higher energy region above 1 TeV, the effect of backscattering gets more and more significant and therefore the helium dominates the total contamination at the highest energy region although it is still sufficiently small not to significantly influence the proton spectrum.

Energy Unfolding

In order to take into account the relatively limited energy resolution, energy unfolding is necessary to correct for bin-to-bin migration effects. For reference, the observed energy fraction is around 35% and the resultant energy resolution is 30–40% in the energy region analyzed here. As an energy unfolding method in this analysis, we used the Bayesian approach implemented in the RooUnfold package [S11, S12] in ROOT [S13], with the response matrix derived using MC simulation. Convergence is obtained within two iterations, given the relatively accurate prior distribution obtained from the previous observations, i.e., AMS-02 [S8] and CREAM-III [S10].

Though CALET calorimeter is homogeneous, practically most of calorimeters are non-compensating to a certain degree. Therefore, a correction for electrons is not necessarily the same as for protons. Because of the limited energy resolution, an absolute energy scale calibration using geomagnetic rigidity cutoff used in Refs. [S1, S4] could not be performed.

Consistency between LE and HE Analyses

Depending on the on-orbit trigger mode and corresponding offline-trigger threshold, two spectra are obtained with the LE and HE analyses, respectively, as shown in Fig. S2. For $E < 200$ GeV, the use of LE-trigger analysis is required because an offline trigger threshold higher than in the hardware trigger was found to introduce an efficiency bias in the HE-trigger analysis, which became evident with a scan of the offline-trigger threshold using LE-trigger data. Since both fluxes are well consistent in $E > 200$ GeV, they are combined around $E \sim 300$ GeV, taking into account the different statistics of the two trigger modes.

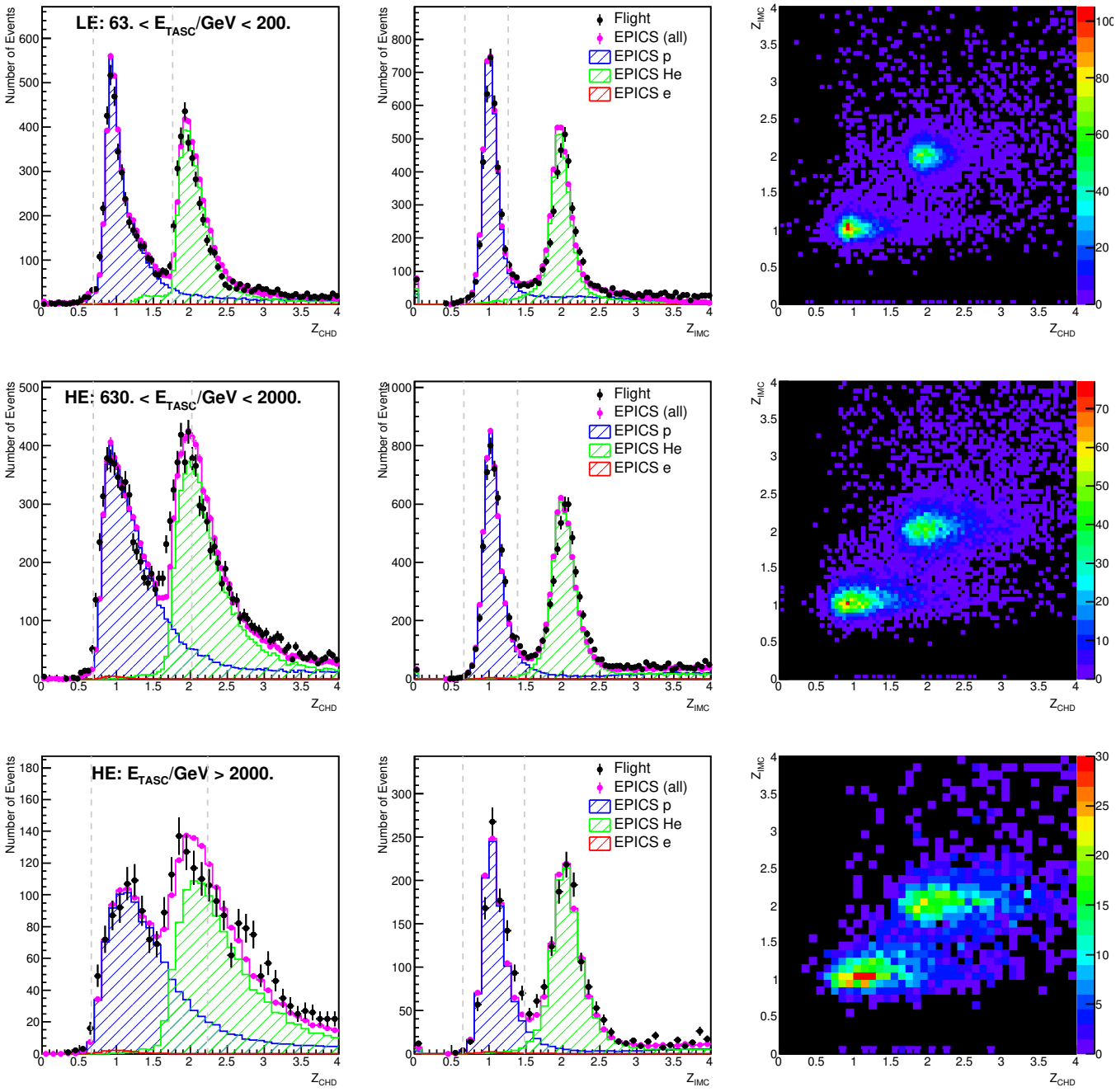


FIG. S1. Examples of CHD/IMC charge distributions. Left, center and right panels show the CHD charge, IMC charge and correlation between CHD and IMC charges, respectively. From top to bottom, the plots corresponds to events with $63 < E_{\rm TASC} < 200$ GeV, $630 < E_{\rm TASC} < 2000$ GeV, and $E_{\rm TASC} > 2000$ GeV, respectively. Gray dashed lines indicate the cut positions at 110 GeV (Top), 1100 GeV (Middle) and 3600 GeV (Bottom).

SYSTEMATIC UNCERTAINTIES

Dominant sources of systematics uncertainties in proton analysis include:

(1) hadronic interaction modeling,

(2) energy response,

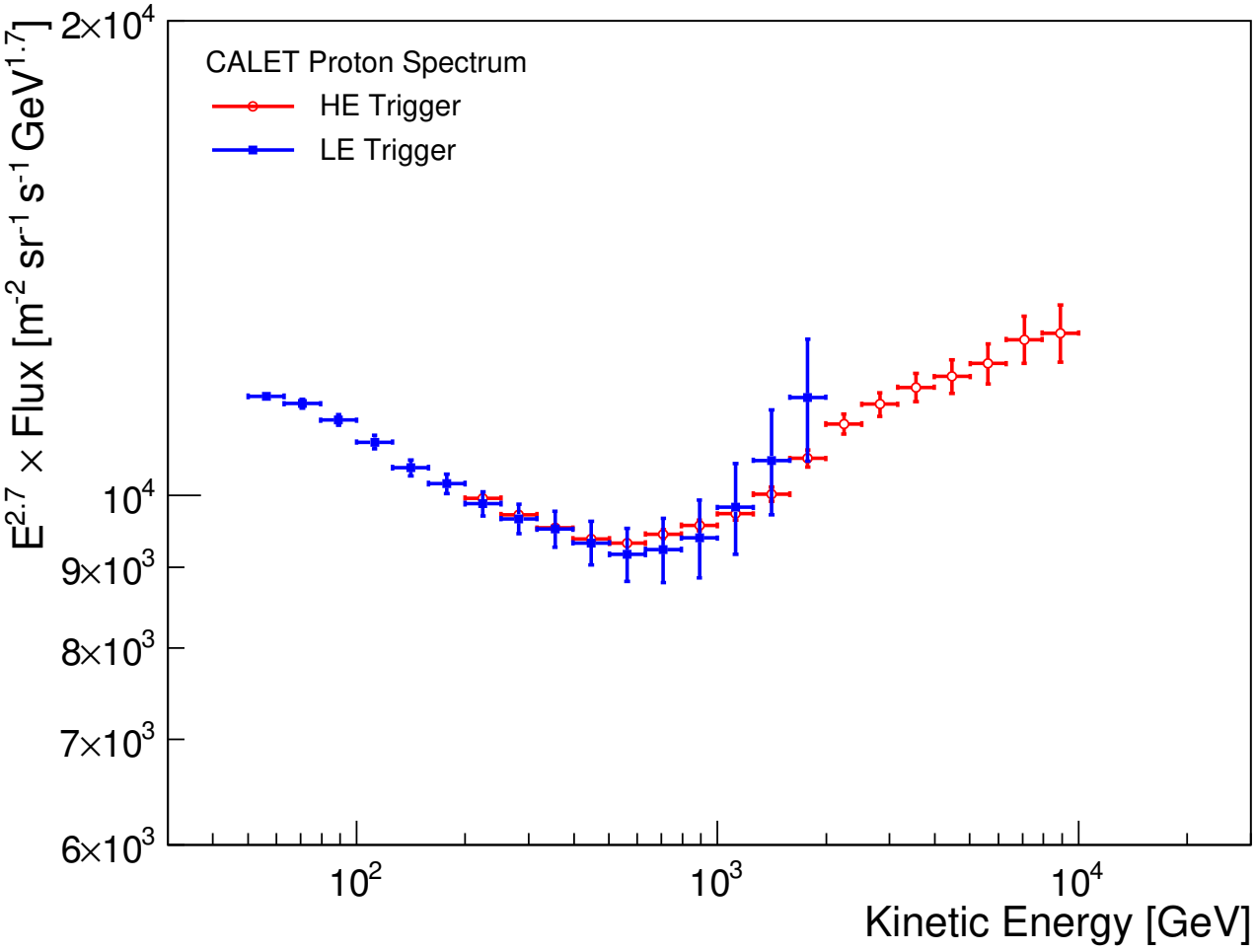


FIG. S2. Proton spectrum from two data sets corresponding to LE-trigger (blue squares) and HE-trigger (red circles) analyses.

(3) track reconstruction, and

(4) charge identification.

To address these uncertainties, various approaches are used and discussed in the following. An important part of systematics comes from the accuracy of the beam test calibration and its extrapolation/interpolation. The stability of the measured spectrum against variations of several analysis cuts is also a crucial tool to estimate the associated uncertainties.

Most of the systematic uncertainties in normalization are taken from the studies performed for the electron analysis. This uncertainty is estimated as 4.1% based on the electron spectrum paper [S1], as the sum in quadrature of the uncertainties on live time (3.4%), radiation environment (1.8%), and long-term stability (1.4%).

Hadronic interaction: The uncertainty in the hadronic interaction affects directly the trigger efficiency and it is also closely connected to the uncertainty in the energy response, as discussed separately in the following. In the low-energy region, the absolute calibration of the trigger efficiency was performed at the beam test. The main source of uncertainty comes from the accuracy of the calibration. In addition to the measurement accuracy, possible systematic bias due to normalization in the measurements of trigger efficiency was considered as a systematic uncertainty and is estimated as 2.2% and 3.3% for HE and LE analyses, respectively.

In the high-energy region, a non-trivial extrapolation from the maximum available beam energy, i.e. 400 GeV, is necessary. To address this uncertainty, the relative differences between different MC models, i.e., FLUKA and Geant4 versus EPICS were investigated as shown in Fig. SS3. In the FLUKA and Geant4 simulation, the same corrections for EPICS were applied, as determined from the beam test data. It should be noted that other effects such as the

difference in backscattering treatment and energy responses are also included in this study. Considering that (i) there is good consistency between LE and HE analyses, (ii) EPICS is directly calibrated with beam test data, (iii) backscattering at higher energies is better simulated in EPICS than in Geant4 and FLUKA [S1] and (iv) the difference in the energy response among the 3 MC models show only little energy dependence one half of the differences have been included in the energy dependent systematics (see the comments in the caption of Fig. SS3). The difference between DPMJET-III (reference) and EPOS was also studied, but it was found to be completely negligible in the energy range considered here, mainly because the use of EPOS is allowed only above 20 TeV.

Energy response: The uncertainty in the energy response is closely related to the uncertainty in the modeling of the hadronic interaction. As in the case of the uncertainty of the trigger efficiency, the absolute calibration of the energy response was performed using the beam test data in the low-energy region. The main source of uncertainty in the energy response comes from the accuracy of the calibration, with dominant contributions from the uncertainty in temperature of $\pm 0.5^o$, which translates into 2.8% energy scale uncertainty.

As in the beam test analysis only 3 TASC logs per layer were used, the difference of the spectrum obtained with energy measurements between 3 TASC logs (the one associated with the track and the two lateral neighbors) and the whole TASC sum (used in this analysis) is considered as the correction factor. In addition to that, one half of the correction is included as upper and lower systematic error.

In the high-energy region, significant extrapolation from the maximum beam energy, i.e. 400 GeV, is necessary, which is taken into account as MC model dependence.

While the beam test correction basically addresses the relation between the primary energy and the mean shower energy, the effect of energy resolution should also be considered. Separate unfolding procedures with TASC energy sum including the log being hit ± 2, ± 3, and ± 5 neighbors are applied and the stability of the spectrum is included in the systematics, where stability is defined as the standard deviation of the relative differences in each energy bin with respect to the reference flux.

Track reconstruction: It is not easy to directly assess the uncertainty in track reconstruction. However, since tracking is the basis of most of the analysis, especially for the track-dependent selection cuts, the effects are evaluated by studying the dependence on the charge cut and some pre-selection cuts, especially (2), (6) and (7). To investigate the uncertainty in the definition of the acceptance, restricted acceptance regions are studied and the resultant fluxes are compared, resulting in negligible differences. Regarding cut (6), efficiencies were varied by $\sim +20\%$, $\sim +10\%$, $\pm 0\%$, $\sim -20\%$, and $\sim -40\%$ (corresponding to 99%, 97%, 95%, 90% and 85% efficiencies for "target" events), and the relative differences with respect to the reference cases were obtained for each energy bin. The standard deviation of the relative differences were considered as systematic uncertainty associated with cut (6). As per cut (7), a tighter cut is used with an efficiency for "target" events of 95% instead of 99%. The relative differences with respect to the nominal case (99% efficiency) are considered as the systematic uncertainty, which are applied to both positive and negative sides.

Charge identification: As helium contamination is one of the main uncertainties in the proton spectrum analysis especially in the high energy region, it is very important to study the flux stability against charge cut efficiencies considering that the contamination ratio from helium may depend on the same cuts. The stability against the charge cut efficiency is shown in Fig. SS4 for LE- and HE-trigger analyses. They are included in the systematic uncertainty.

Total systematic uncertainty: Considering all of the above contributions, blue long-dashed and red solid lines of Fig. SS4 show the total systematic uncertainty for LE and HE analyses, respectively, as a function of primary energy in the proton spectrum analysis. For reference, a breakdown of the individual energy dependent systematic uncertainties in LE and HE analyses is shown in Fig. SS5.

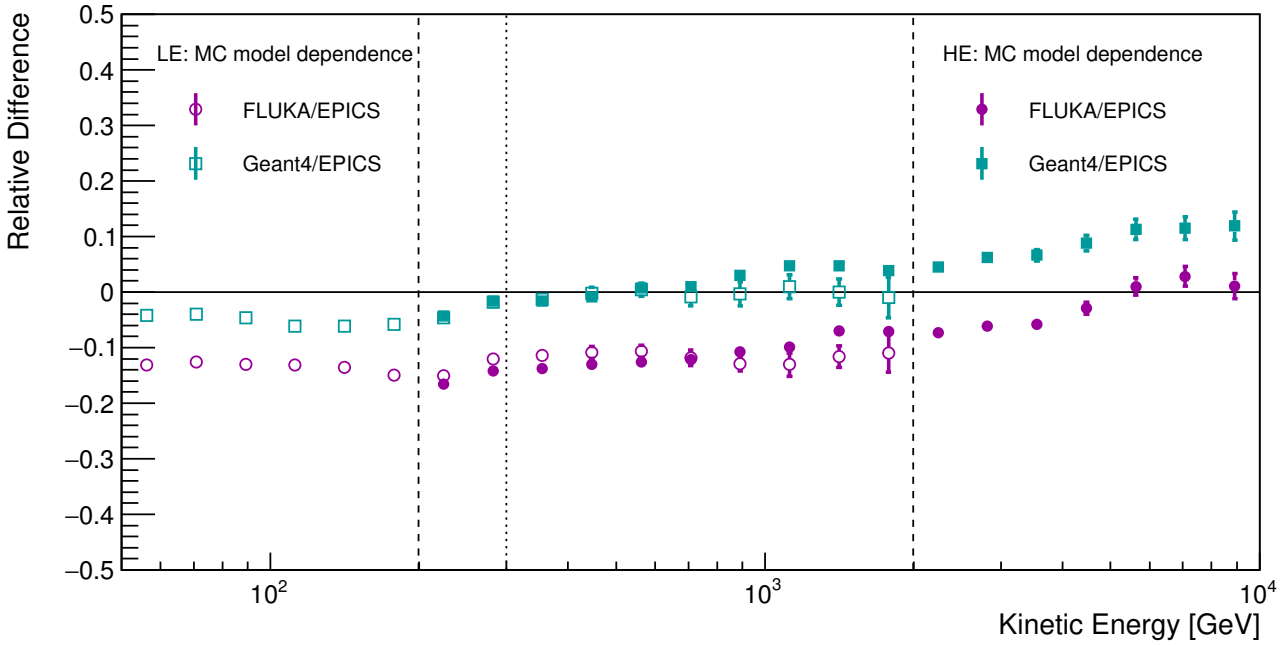


FIG. S3. Relative difference of the measured flux when different MC simulations are used with respect to the EPICS case. FLUKA/EPICS and Geant4/EPICS are shown as magenta circles and cyan squares, respectively. Open (closed) symbols are used for LE-trigger (HE-trigger) analysis. The upper (lower) bound of the energy region used in LE (HE) analysis is shown by the dashed line on the left (right) side of the picture. The two analyses are combined at 300 GeV as indicated by dotted line. The relatively larger difference between FLUKA and EPICS appears to be caused by different normalization as FLUKA and Geant4 curves are practically parallel. Considering the fact that EPICS has been validated with beam-test measurements in the low-energy region, we have conservatively attributed one-half of the difference between FLUKA/Geant4 and EPICS as energy dependent systematic uncertainty.

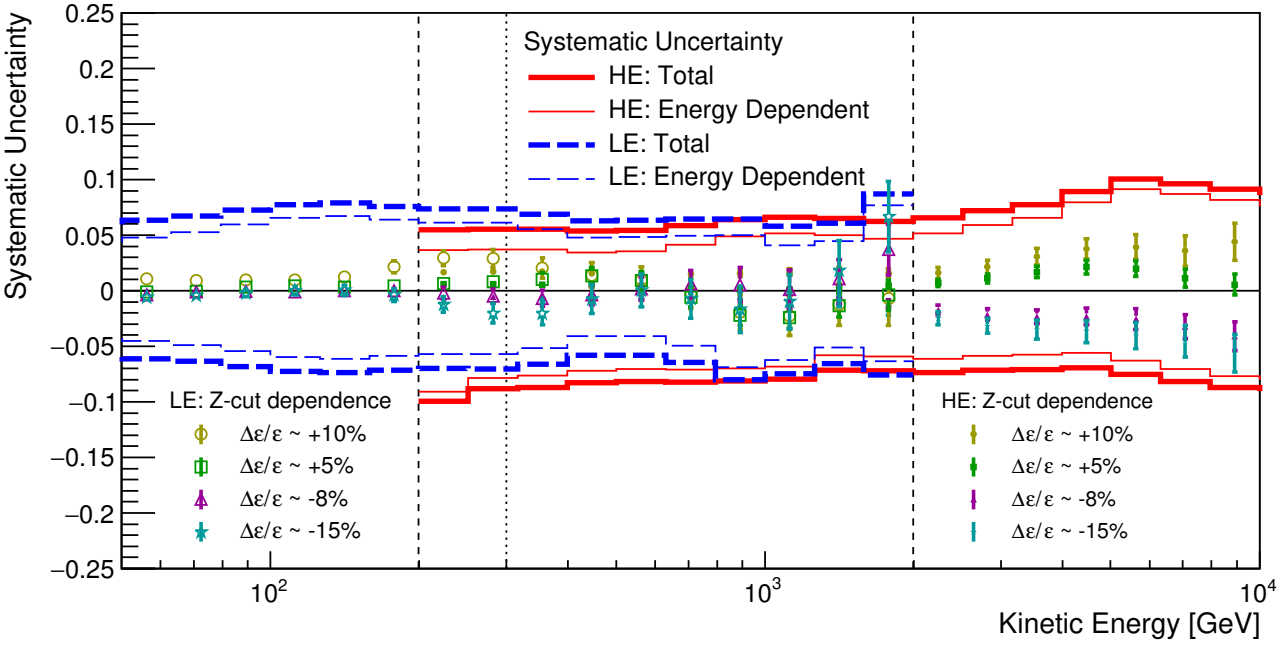


FIG. S4. Energy dependence of total systematic uncertainty band (thick lines). Contributions from energy dependent systematic uncertainty are shown as thinner lines of the same color. Blue long-dashed lines and red solid lines correspond to LE- and HE-trigger analyses, respectively. Relative differences of the measured flux in the case of different charge selections with respect to the nominal charge cut (the efficiency variation considered here ranges from $\sim -15\%$ to $\sim +10\%$) are also shown. The standard deviation of the relative differences is taken as energy dependent systematic uncertainty in each energy bin. The total uncertainty is the quadratic sum of energy dependent and normalization uncertainties. The upper (lower) bound of the energy region used in LE (HE) analysis is shown by the dashed line on the left (right) side of the picture. The two analyses are combined at 300 GeV as indicated by dotted line.

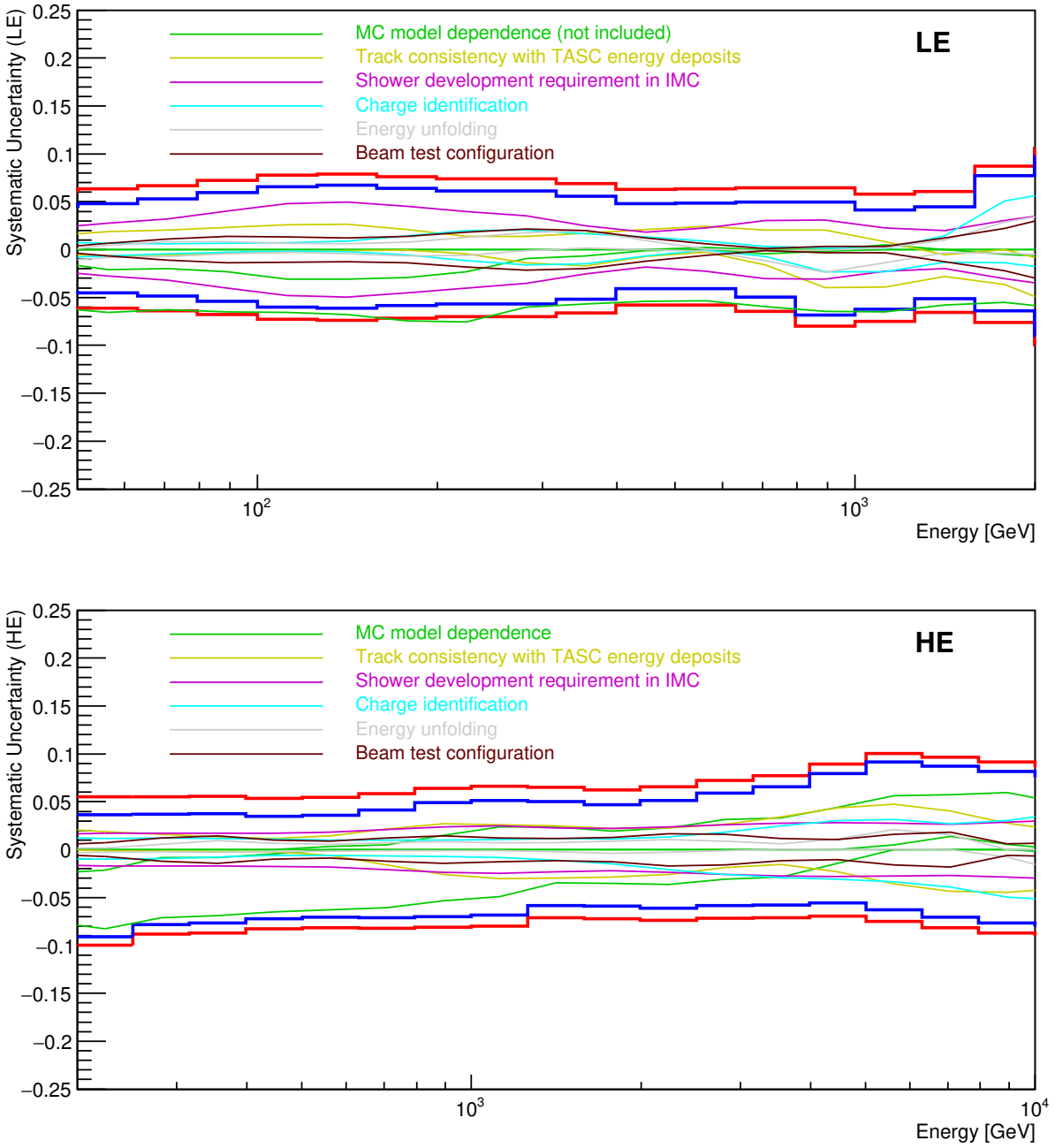


FIG. S5. Summary of energy dependent systematic uncertainties for LE-trigger (upper figure) and HE-trigger (lower figure) analysis, where the energy dependence of total systematic uncertainty bands are shown by the thick red lines, while the thick blue lines isolate the total contribution from systematic uncertainties with an energy dependence. Thin lines with other colors show the contributions from each component as explained in the legend. The energy dependent systematic uncertainty includes the contributions from trigger efficiency which is estimated as 3.3% and 2.2% for LE and HE analyses, respectively.

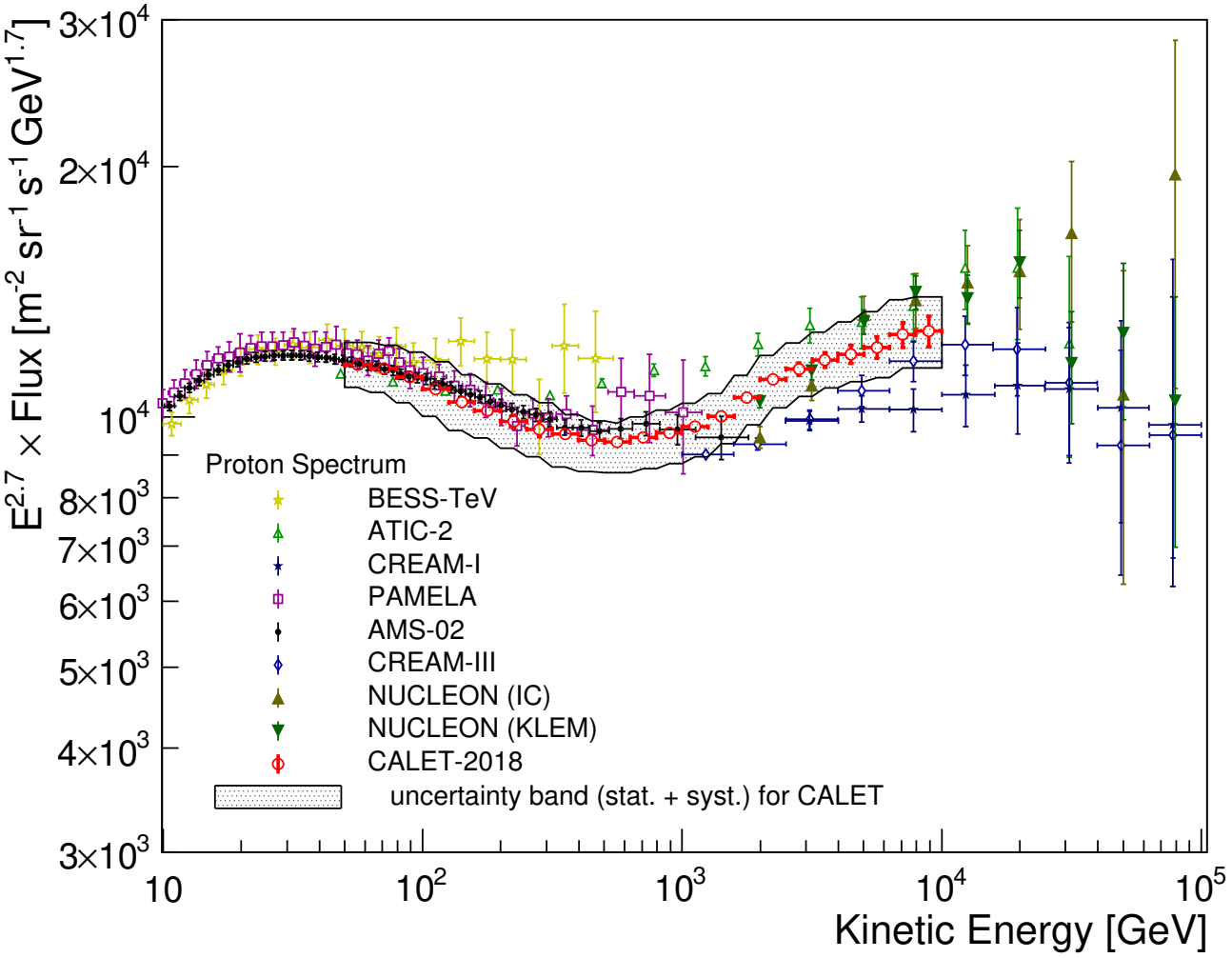


FIG. S6. Cosmic-ray proton spectrum measured by CALET from 50 GeV to 10 TeV using an energy binning of 10 bins per decade. The gray band indicates the quadratic sum of statistical and systematic errors. Also plotted are recent direct measurements in space [S14–S17] and from high altitude balloons [S4, S10, S18, S19].

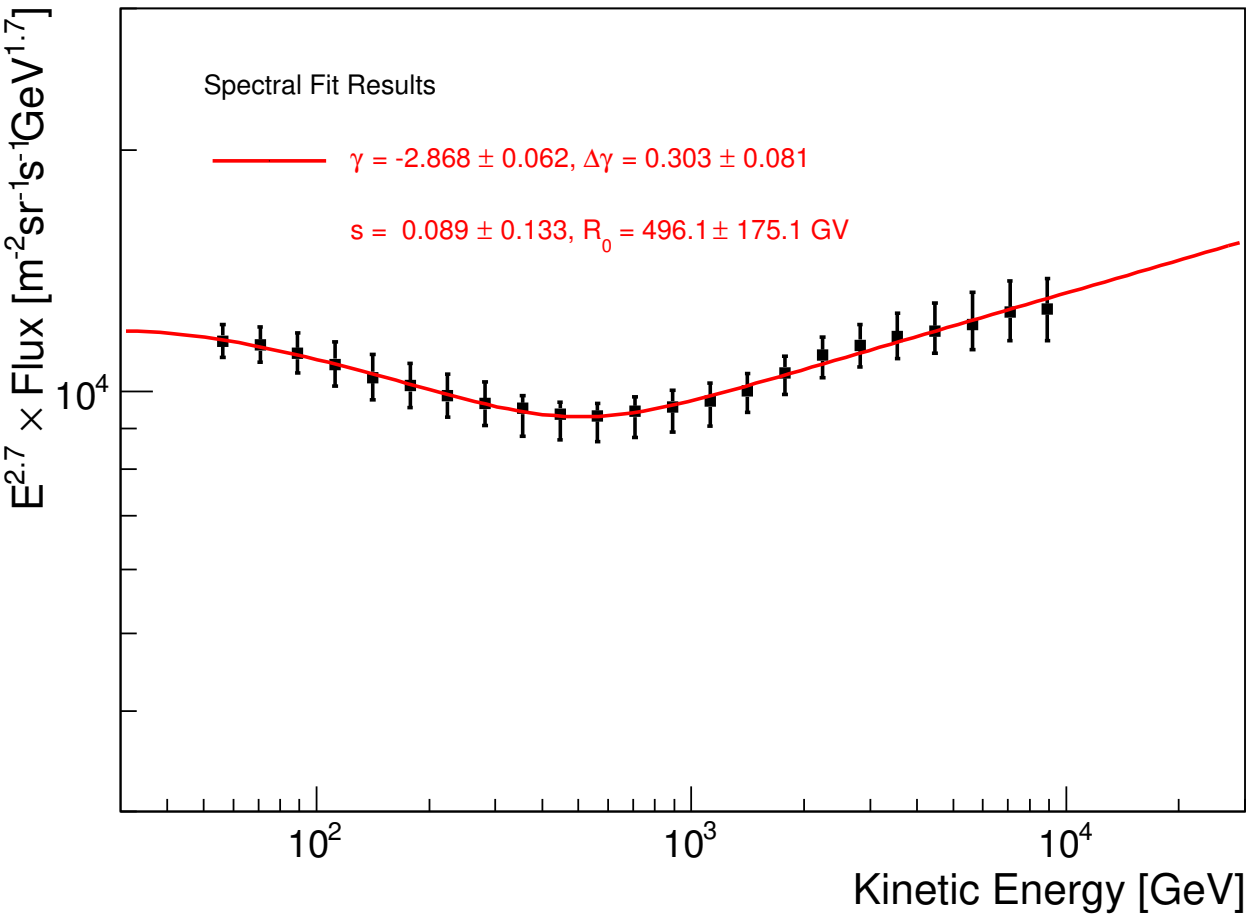


FIG. S7. Fit of the CALET proton spectrum with a smoothly broken power-law function as defined in Eq. (3) of Ref. [S14]. Statistical errors are shown in quadrature with systematic errors including only energy dependent ones, neglecting to first order possible correlations among different sources of systematic errors and assuming that they are normally distributed. The fit parameters are given in the plot. Since the fit is performed as a function of rigidity, an appropriate change of variables is carried out in the fitting function. The softer value of the spectral index obtained in this smooth fit with respect to the single power-law fit in the 50-500 GeV energy interval is mainly due to the inclusion of a solar modulation potential of 550 MV (fixed) using the force field approximation [S21]. The stability of the result versus the choice of the potential has been studied by varying its value from 450 MV to 650 MV. The result has been found to be insensitive within errors, differing at most by 0.01 for γ and $\Delta\gamma$.

TABLE I. Table of CALET proton spectrum. Energy in each bin is simply represented by geometric mean. The first and second errors associated with mean energy represent systematic error in global energy scale and potentially energy dependent ones, respectively. Energy dependent energy scale error mainly comes from beam test in the lower energy region and energy calibration of lower gain range [S2] in the higher energy region. For the flux the first, second and third errors represent the statistical uncertainties (68% confidence level), systematic uncertainties in normalization, and energy dependent systematic uncertainties, respectively.

Energy Bin (GeV)	Representative Energy (GeV)	Flux ($m^{-2}sr^{-1}s^{-1}GeV^{-1}$)
50.1–63.1	$56.2 \pm 1.6 \pm 0.6$	$(2.176 \pm 0.012 \pm 0.089^{+0.105}_{-0.099}) \times 10^{-1}$
63.1–79.4	$70.8 \pm 2.0 \pm 0.7$	$(1.157 \pm 0.008 \pm 0.048^{+0.061}_{-0.056}) \times 10^{-1}$
79.4–100.0	$89.1 \pm 2.5 \pm 0.9$	$(6.064 \pm 0.047 \pm 0.249^{+0.361}_{-0.329}) \times 10^{-2}$
100.0–125.9	$112.2 \pm 3.1 \pm 1.1$	$(3.153 \pm 0.030 \pm 0.130^{+0.207}_{-0.189}) \times 10^{-2}$
125.9–158.5	$141.3 \pm 4.0 \pm 1.4$	$(1.631 \pm 0.019 \pm 0.067^{+0.110}_{-0.100}) \times 10^{-2}$
158.5–199.5	$177.8 \pm 5.0 \pm 1.8$	$(8.558 \pm 0.122 \pm 0.352^{+0.546}_{-0.501}) \times 10^{-3}$
199.5–251.2	$223.9 \pm 6.3 \pm 2.3$	$(4.463 \pm 0.078 \pm 0.183^{+0.274}_{-0.253}) \times 10^{-3}$
251.2–316.2	$281.8 \pm 7.9 \pm 2.9$	$(2.345 \pm 0.050 \pm 0.096^{+0.143}_{-0.133}) \times 10^{-3}$
316.2–398.1	$354.8 \pm 9.9 \pm 3.6$	$(1.242 \pm 0.004 \pm 0.051^{+0.046}_{-0.095}) \times 10^{-3}$
398.1–501.2	$446.7 \pm 12.5 \pm 4.5$	$(6.565 \pm 0.029 \pm 0.270^{+0.228}_{-0.472}) \times 10^{-4}$
501.2–631.0	$562.3 \pm 15.7 \pm 5.8$	$(3.505 \pm 0.018 \pm 0.144^{+0.125}_{-0.247}) \times 10^{-4}$
631.0–794.3	$707.9 \pm 19.8 \pm 7.5$	$(1.907 \pm 0.012 \pm 0.078^{+0.079}_{-0.136}) \times 10^{-4}$
794.3–1000.0	$891.3 \pm 25.0 \pm 10.2$	$(1.037 \pm 0.008 \pm 0.043^{+0.051}_{-0.072}) \times 10^{-4}$
1000.0–1258.9	$1122.0 \pm 31.4 \pm 14.5$	$(5.665 \pm 0.050 \pm 0.233^{+0.292}_{-0.387}) \times 10^{-5}$
1258.9–1584.9	$1412.5 \pm 39.6 \pm 20.4$	$(3.131 \pm 0.033 \pm 0.129^{+0.157}_{-0.182}) \times 10^{-5}$
1584.9–1995.3	$1778.3 \pm 49.8 \pm 27.8$	$(1.772 \pm 0.023 \pm 0.073^{+0.083}_{-0.105}) \times 10^{-5}$
1995.3–2511.9	$2238.7 \pm 62.7 \pm 36.9$	$(1.001 \pm 0.015 \pm 0.041^{+0.051}_{-0.061}) \times 10^{-5}$
2511.9–3162.3	$2818.4 \pm 78.9 \pm 48.4$	$(5.531 \pm 0.095 \pm 0.227^{+0.328}_{-0.324}) \times 10^{-6}$
3162.3–3981.1	$3548.1 \pm 99.3 \pm 62.9$	$(3.044 \pm 0.063 \pm 0.125^{+0.200}_{-0.176}) \times 10^{-6}$
3981.1–5011.9	$4466.8 \pm 125.1 \pm 81.4$	$(1.661 \pm 0.041 \pm 0.068^{+0.132}_{-0.093}) \times 10^{-6}$
5011.9–6309.6	$5623.4 \pm 157.5 \pm 104.8$	$(9.090 \pm 0.266 \pm 0.374^{+0.832}_{-0.571}) \times 10^{-7}$
6309.6–7943.3	$7079.5 \pm 198.2 \pm 134.9$	$(5.056 \pm 0.174 \pm 0.208^{+0.441}_{-0.356}) \times 10^{-7}$
7943.3–10000.0	$8912.5 \pm 249.6 \pm 172.3$	$(2.741 \pm 0.115 \pm 0.113^{+0.224}_{-0.210}) \times 10^{-7}$

* yoichi.asaoka@aoni.waseda.jp
† piersimone.marrocchesi@pi.infn.it
‡ torii.shoji@waseda.jp

[S1] O. Adriani *et al.* (CALET Collaboration), Phys. Rev. Lett. **119**, 181101 (2017) .
[S2] Y. Asaoka, Y. Akaike, Y. Komiya, R. Miyata, S. Torii, *et al.* (CALET Collaboration), Astropart. Phys. **91**, 1 (2017) .
[S3] Y. Asaoka, Y. Ozawa, S. Torii, *et al.* (CALET Collaboration), Astropart. Phys. **100**, 29 (2018) .
[S4] O. Adriani *et al.* (CALET Collaboration), Phys. Rev. Lett. **120**, 261102 (2018) .
[S5] P. Maestro, N. Mori, *et al.* (CALET Collaboration), in *Proceeding of Science (ICRC2017) 208* (2017) .
[S6] P. S. Marrocchesi *et al.* (CALET Collaboration), in *Proceeding of Science (ICRC2017) 156* (2017) .
[S7] P. Brogi *et al.* (CALET Collaboration), in *Proceedings of Science (ICRC2015)* (2015) p. 585 .
[S8] M. Aguilar *et al.* (AMS Collaboration), Phys. Rev. Lett. **114**, 171103 (2015) .
[S9] M. Aguilar *et al.* (AMS Collaboration), Phys. Rev. Lett. **115**, 211101 (2015) .
[S10] Y. Yoon *et al.*, Astrophys. J. **839**, 5 (2017) .
[S11] T. Adye, in *arXiv:1105.1160v1* (2011) .
[S12] G. D'Agostini, *Nucl. Instrum. Methods Phys Res., Sect. A*, **362**, 487 (1995) .
[S13] R. Brun and F. Rademakers, *Nucl. Instrum. Methods Phys Res., Sect. A*, **389**, 81 (1997) .
[S14] M. Aguilar *et al.* (AMS Collaboration), Phys. Rev. Lett. **114**, 171103 (2015) .
[S15] O. Adriani *et al.*, Phys. Rept. **544**, 323 (2014) .
[S16] O. Adriani *et al.*, Riv. Nuovo Cim. **40**, 1 (2017) .

[S17] E. Atkin *et al.*, JETP Letters **108**, 5 (2018) .
[S18] S. Haino *et al.*, Phys. Lett. B **594**, 35 (2004) .
[S19] A. Panov *et al.*, Bull. Russ. Acad. Sci. Phys. **71**, 494 (2007) .
[S20] Y. Yoon *et al.*, Astrophys. J. **728**, 122 (2011) .
[S21] L. Glesson and W. Axford, Astrophys. J. **154**, 1011 (1968) .